Hindawi
Journal of Chemistry
Volume 2021, Article ID 6678588, 14 pages
https://doi.org/10.1155/2021/6678588

Research Article

Synthesis and Characterization of Magnetic Fe_3O_4/Zeolite NaA Nanocomposite for the Adsorption Removal of Methylene Blue Potential in Wastewater Treatment

Ngoc Bich Thi Tran,[1] **Ngoc Bich Duong**,[2] **and Ngoc Long Le**[3,4]

[1]*School of Agriculture and Aquaculture, Tra Vinh University, 126 Nguyen Thien Thanh, Tra Vinh 940000, Vietnam*
[2]*School of Engineering and Technology, Tra Vinh University, 126 Nguyen Thien Thanh, Tra Vinh 940000, Vietnam*
[3]*Department of Metallic Materials, Faculty of Materials Technology, Ho Chi Minh City University of Technology (HCMUT), 268 Ly Thuong Kiet Street, Ward 14, District 10, Ho Chi Minh City 700000, Vietnam*
[4]*Vietnam National University Ho Chi Minh City, Linh Trung Ward, Thu Duc District, Ho Chi Minh City 700000, Vietnam*

Correspondence should be addressed to Ngoc Long Le; lengoclong.bk@gmail.com

Received 11 November 2020; Revised 21 January 2021; Accepted 23 January 2021; Published 1 February 2021

Academic Editor: Liviu Mitu

In this research, the magnetic Fe_3O_4/zeolite NaA nanocomposite (Fe_3O_4/ZA), Fe_3O_4 nanoparticles, and zeolite NaA have been synthesized by facile hydrothermal methods for adsorption removal of methylene blue from aqueous solution. The as-synthesized Fe_3O_4/ZA nanocomposite was characterized by X-ray diffraction (XRD), MicroRaman analysis, Fourier-transform infrared (FTIR) spectroscopy, scanning electron microscopy (SEM), energy-dispersive X-ray (EDX) spectroscopy, X-ray fluorescence (XRF), N_2 adsorption isotherms (BET), and UV-VIS analysis. The results show that with a small weight loading of Fe_3O_4, the ~3.3% Fe_3O_4/ZA sample exhibits a high adsorption capacity (~40.36 mg·g^{-1}) and removal efficiency (~96.8%) compared to that of the zeolite NaA (~32.99 mg·g^{-1} and 79.11%, respectively). Interestingly, the removal efficiency and the adsorption capacity increase rapidly with the increase of adsorption time (10–60 minutes) and Fe_3O_4 loading (~3.3–9.3% wt.) in the Fe_3O_4/ZA composition. The adsorption mechanism of MB molecules of the Fe_3O_4/ZA can be addressed at the combination of the interaction between active sites on the surfaces and edges of the invert spinel ferrite Fe_3O_4 nanoparticles and zeolite NaA with MB molecules. Our approach provides a simple, efficient, and scalable synthesis process that render practical applications of the magnetic Fe_3O_4/ZA nanocomposite as a lower-cost adsorbent for wastewater treatment.

1. Introduction

Water is one of the most important resources essential for all living organisms. However, due to the fast growing in production of textile and plastics industries, methylene blue became the byproduct of the fabrication processes and is considered a contaminant that remains untreated in wastewater. Methylene blue (MB) (3, 7-bis (dimethylamino)-phenothiazin-5-iumchloride) is a thiazine cationic dye which is commonly used for biological staining also and coloring paper, hair, cottons, and wools [1]. The accumulation of MB in wastewater may cause many health effects in breathing, vomiting, eye burns, diarrhea, and nausea [2] and negative impacts to the environment. In the recent years, such methods as flocculation [3], membrane filtration [4], oxidation [5], photocatalytic degradation [6], and adsorption [7] have been developed for removing MB from abovementioned wastewater. Among these techniques, adsorption stands out to be a suitable approach that is capable of separating organic molecules by using adsorbent materials. Previous reports showed that MB can be adsorptive and removed from aqueous solution by using activated carbon obtained from Pea Shells [8] or corn husk [9], biomass fabricated from Algae *D. Antarctica* [10], agricultural residue walnut shell [11], and zeolite-based materials [12–14].

Zeolites are aluminosilicate minerals which are classified as porous materials due to their crystalline microstructures possess cages, channels, and open void spaces within their frameworks [15]. Zeolite frameworks are constructed by $[SiO_4]^{4-}$ and $[AlO_4]^{5-}$ tetrahedral, linked together to form cages connected by pore openings of defined size. The presence of $[AlO_4]^-$ in the zeolite framework introduces negative charges which is balanced by cations such as Ca^{2+}, K^+, and Na^+ [16]. Previous studies show that zeolite materials possess good adsorption efficiency for removal of heavy metals like arsenic [17], mercury [18], fluoride [19], and organic dyes [20] as adsorbents. Zeolite NaA [21], with chemical composition $[Na_{12}\,[(AlO_2)_{12}\,(SiO_2)_{12}]$. 27 H_2O, is identified by the Al/Si ratio of ~1.0. Zeolite NaA is currently a commercially important zeolite used in the industry for catalysis, adsorption, and industrial gas separations. However, difficulty in separating the adsorbed zeolite from the aqueous solution remains a considerable problem. In industries, magnetic separation is desirable due to its advances in operation compare to filtration, centrifugation, or gravitational separation.

On the other hand, magnetic iron oxide-based materials have attracted much attention in many environmental applications. Among them, invert spinel-structured Fe_3O_4 oxide possesses high chemical stability, high coercively, low Curie temperature, and low toxicity [22]. Due to their magnetic property, the Fe_3O_4 solid phase can be separated easily from adsorbed liquid medium by using magnetic separation. Several synthesis methods such as the microemulsion technique [23], electrochemical synthesis [24], hydrothermal method [25], sol-gel process [26], and coprecipitation synthesis [27] exist for synthesizing magnetic Fe_3O_4 materials. Among the abovementioned methods, the hydrothermal approach is an effective method to fabricate nanoparticle size materials within a short time [28].

In this research, we employed a facile hydrothermal synthesis method to synthesize magnetite Fe_3O_4/zeolite NaA nanocomposite (denoted as Fe_3O_4/ZA) as low-cost adsorbents for the removal of MB from aqueous solutions. The advantages of magnetic adsorbents are magnetic separation capability that can be easily separated from the solution by applying an external magnet. The as-synthesized Fe_3O_4/ZA nanocomposite was characterized using XRD, Micro-Raman, FTIR, EDX, XRF, and FESEM to investigate the formation of magnetite Fe_3O_4/ZA nanocomposite samples. Their adsorption capacity for removal of MB organic molecules was conducted by bath adsorption experiments and investigated using UV-VIS absorbance analysis. Our approach provides a simple, efficient, and scalable synthesis process that renders practical applications of the as-synthesized magnetic Fe_3O_4/ZA nanocomposite for wastewater treatment.

2. Materials and Methods

2.1. Chemicals and Materials. The analytical graded chemicals were used without purification. The main chemicals used include sodium silicate solution (Na_3SiO_3 30% SiO_2), aluminum hydroxide (Al $(OH)_3$ 99%), sodium hydroxide (NaOH, 99%), hydrochloric acid (HCl, 99%), iron (II) chloride tetrahydrate ($FeCl_2.4H_2O$, 99%), iron (III) chloride hexahydrate ($FeCl_3.6H_2O$, 98%), methylene blue (MB) ($C_{16}H_{18}ClN_3S.xH_2O$, >82%), ammonia (NH_4OH, 32%), and hydrochloric acid (HCl, 0.1 M) solutions obtained from Sigma Aldrich (Singapore).

2.2. Preparation of Zeolite NaA. Zeolite NaA was prepared by hydrothermal method as described in [29] with modification. In brief, sodium silicate (SiO_2 source) and aluminum hydroxide (Al_2O_3 source) were dissolved separately in deionized water and sodium hydroxide solution. The SiO_2 and Al_2O_3 sols were formed when the sodium silicate and aluminum hydroxide was dissolved in sodium hydroxide solution and followed by filtration to remove the insoluble residues. The molar ratios of SiO_2/Al_2O_3, Na_2O/SiO_2, and H_2O/Na_2O are controlled at ~1.3, 1.5, and 160, respectively. After that, these as-prepared solutions were ultrasonic-assisted mixed together and transferred to a Teflon-lined stainless steel autoclave reactor and sealed and heated at ~120 ± 5°C for 6 hours. The obtained solid phase was collected and washed with distillated water until the pH value reached 8.0 and dried overnight at ~105°C.

2.3. Preparation of Magnetic Fe_3O_4 Nanoparticles. Magnetic Fe_3O_4 nanoparticles (denoted as Fe_3O_4 NPs) were synthesized by the hydrothermal method [25] from an alkaline solution of Fe^{2+} and Fe^{3+} salts. In brief, a solution of $FeCl_2$ and $FeCl_3$ with Fe^{2+}/Fe^{3+} molar ratio of ~1/2 was mixed at room temperature under ultrasonication condition. After that, ammonia solution (~30%) was added dropwise to control pH of the as-prepared solution in range of ~8.0–9.0. The final solution was transferred to a Teflon-lined stainless steel autoclave reactor and sealed and crystallized at ~120 ± 5°C for 3 hours. After the reaction process, the black precipitation was collected and washed several times with deionized water.

2.4. Synthesis of Fe_3O_4/ZA Nanocomposite. For the synthesis of Fe_3O_4/ZA nanocomposite, an amount of ~6.0 g of as-prepared zeolites A was dispersed into 100 mL of distilled water and sonicated for ~30 minutes. Next, a volume ~20 mL of $FeCl_3$ and $FeCl_2$ solutions (molar ratio of Fe^{2+}/Fe^{3+} is 1/2) was added into the as-prepared suspension. Then, about ~10 mL of a 1.0 M NaOH solution was added dropwise under ultrasonication condition in other to control thevpH of this solution in range of ~8.0–9.0. After that, these solutions were ultrasonic-assisted mixed together and transferred to a 150 mL Teflon-lined stainless steel autoclave reactor (~80 % volume filled) and sealed and heated at ~120 ± 5°C for 6 hours. The obtained solid phase was collected by centrifugation for characterization and washed with distillated water until the pH value reached 8.0 and dried overnight at ~105°C.

To investigate the effect of Fe_3O_4 NP loading to the adsorption capability of the as-synthesized Fe_3O_4/ZA

nanocomposite, different molar ratios of (Fe^{2+}/Fe^{3+}) in the precursors were varied while the amounts of zeolites A in the precursor were kept constant. The Fe_3O_4 NP loading in the Fe_3O_4/ZA nanocomposite samples were designed to be about ~3.3, 6.6, and 9.3 wt. %. The percentage of Fe_3O_4 loading p_F (%) is calculated by the following equation:

$$\text{percentage of } Fe_3O_4 \text{ NPs (\%)}, p_F = \frac{m_{Fe_3O_4}}{m_{Fe_3O_4} + m_{ZA}} \times 100, \quad (1)$$

whereas $m_{Fe_3O_4}$ denotes for the weight of Fe_3O_4 solid phase forming from the synthesis process obtained from XRF data and m_{ZA} is the weight of zeolite A. The final products were used for the structural characterization and bath adsorption experiment investigation.

2.5. Structural Characterization. The X-ray diffraction (XRD) patterns were recorded using a Bruker D8 Advance diffractometer with Cu ($K\alpha$) radiation ($\lambda = 1.5406$ Å). The morphology of the samples was observed by field-emission scanning electron microscopy (FESEM) (S-4800, Hitachi). Elemental compositions were estimated using energy-dispersive X-ray (EDX) spectroscopy and Zeiss EVO LS10 scanning electron microscopy (SEM) equipped with the Oxford INCA ADAX detector. Chemical composition was determined by employing the X-ray fluorescence (XRF) method on a S6 JaAGUAR instrument, Bruker. Micro-Raman measurements were carried out using Horiba XploRA ONE spectrometer equipped with Olympus BX50 microscope attachment to focus the laser beam on a $180 \times 120\ \mu m^2$ selected area of the sample. A green argon laser ($\lambda = 532$ nm, 15 mW) was used as an excitation source with exposition time of 15 seconds and 900 lines per mm grating monochromator with liquid nitrogen-cooled CCD. Fourier-transform infrared spectra (FTIR) in range of 400–4000 cm^{-1} were recorded using a Frontier FT-IR/NIR spectrophotometer, PerkinElmer. UV-VIS absorbance spectra in range of 200–800 nm were obtained by employing Cary 60 UV-VIS spectrophotometer, Agilent Technologies. Low-temperature N_2 adsorption isotherms were employed to determine the specific surface area S_{BET} ($m^2 \cdot g^{-1}$) of the as-synthesized samples using NOVA 1000e Autosorb-1 (Quanta-Chrome Instruments) equipped with NovaWin data acquisition software. The pH value of all the investigated solution was measured by HI2020 edge® Multiparameter pH Meter, Hanna Instruments.

2.6. Batch Adsorption Experiments. In this research, we investigate the potential of the as-synthesized Fe_3O_4/ZA nanocomposite as an adsorbent for removing methylene blue (MB) molecules from solution. In our experiments, the MB solution was prepared by dissolving ~0.300 g·MB powder in ~1.0 L double-distilled water and used as pollutant for bath adsorption experiments. The initial concentration and pK_a of MB solution are $C_o = 300$ mg·L^{-1} and 3.8, respectively.

In the typical bath adsorption experiment, a volume ~50.0 mL of the MB solution was added into 50 mL polypropylene graduated centrifuge tubes with screw cap. Then, an amount ~0.360 g of the Fe_3O_4/ZA nanocomposite with different loading (3.3%, 6.6%, and 9.3%) of Fe_3O_4 NPs was added to this solution. The pH of solutions was kept at ~8.60 by adding NH_4OH and HCl (0.1 M) solutions. After that, the tubes were placed on an isothermal vibrator (HY-4A Cycling Vibrator, Sinosource Ltd.) with a rate of 300 rpm and temperature of ~25°C and kept for 30 minutes. These solutions were centrifuged at 6300 rpm (using an EBA 200S Centrifuge, Hettich) to separate the solid phase from solutions, and the upper (80% vol.) supernatant were collected. The remained concentration of MB left in the collected supernatants was monitored by evaluating the maximum absorption in UV-VIS spectra of the corresponding samples. The MB removal efficiency R (%) and the adsorption capacity q_e (mg·g^{-1}) of the Fe_3O_4/ZA nanocomposite and ZA were calculated using the following equations:

$$\text{removal efficiency (\%)}, R = \frac{C_o - C_e}{C_o} \times 100, \quad (2)$$

$$\text{adsorption capacity } \left(\text{mg} \cdot \text{g}^{-1}\right), q_e = \frac{C_o - C_e}{m} V = \frac{VC_o}{100m} R, \quad (3)$$

$$\text{removal efficiency (\%)}, R = \frac{a_o - a_e}{a_o} \times 100, \quad (4)$$

where C_o (mg·L^{-1}) is the initial concentration of MB; C_e (mg·L^{-1}) is the MB concentration at equilibrium condition of each experiment, V (L) is the volume of MB solution, and m (g) is the weight of the Fe_3O_4/ZA nanocomposite and ZA samples used in experiments. In addition, the absorbance A (a.u.) and the concentration C_e (mol·L^{-1}) of MB solution are linearly related by the BeerLambert law, according to the following equation:

$$A = \varepsilon l C, \quad (5)$$

where ε (L·mol^{-1}·cm^{-1}) is the molar absorptivity of MB ($\varepsilon = 95000$ L·mol^{-1}·cm^{-1}) [30], l (cm) is the optical path length of solution. In addition, the initial (a_o) and equilibrium adsorption (a_e) of MB and can be calculated by sum of area under the fitted peaks in the UV-VIS absorbance spectra of the supernatants collected from bath adsorption experiments, as described in the following equation:

$$A = \sum_i a_{\lambda i}, \quad (6)$$

where $a_{\lambda i}$ are the areas under the characteristic absorbed peaks centered at maximum wavelength λ_i (nm). Under our experimental conditions, by applying the Voigt fitting function (using OriginPro® 8.0 software), the absorbance spectrum of MB exhibits six main characteristic peaks centered at monochromatic wavelengths (λ_i) of ~246, 292, 498, 572, 617, and 664 nm, which is the one employed in most literatures [1, 2, 20], as seen in Figure 1. Therefore, the MB removal efficiency R (%) was calculated using equation (4).

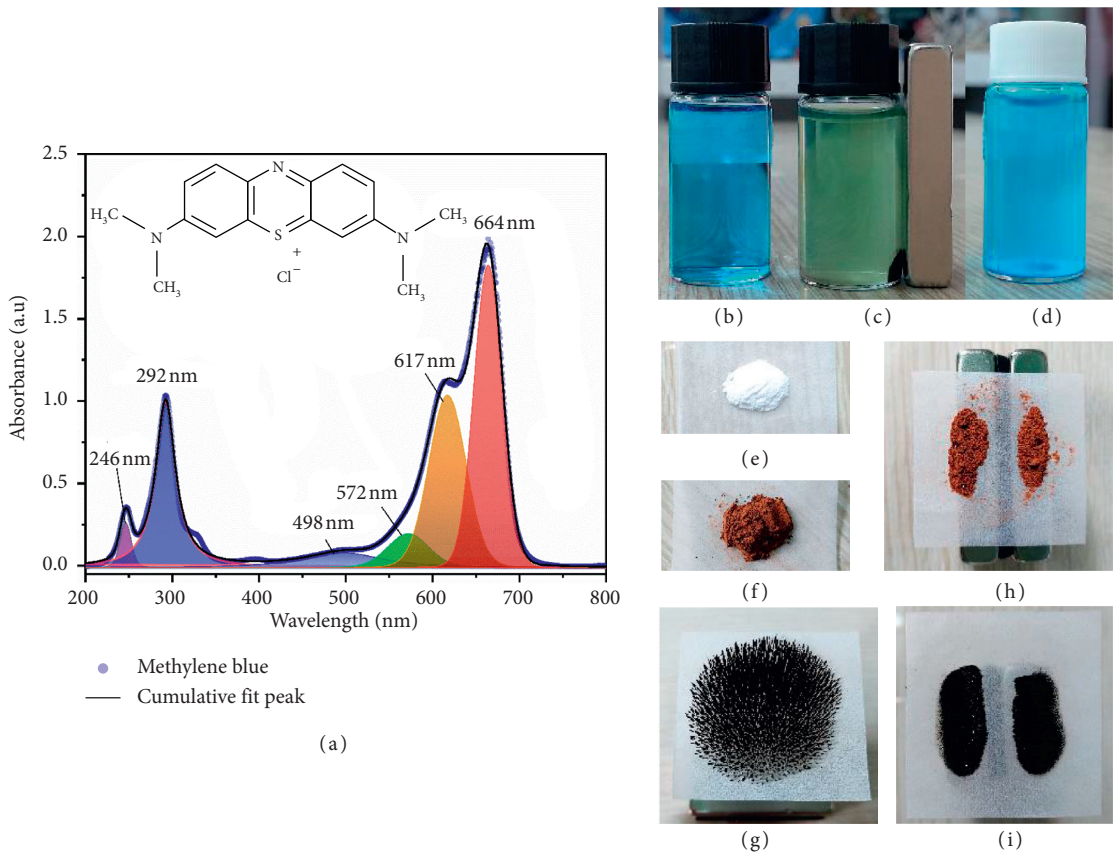

FIGURE 1: UV-VIS absorbance spectrum of the as-prepared methylene blue solution with characteristic peaks fitting results (a); photograph images of (b) initial MB solution; MB solution treated with the as-synthesized Fe_3O_4/ZA nanocomposite (c) and with zeolite NaA (d); photograph images of (e) zeolite NaA; Fe_3O_4/ZA nanocomposite (without applied magnetic field) (f); Fe_3O_4 NP (g, i); Fe_3O_4/ZA nanocomposite and samples (under applied magnetic field) (h).

The bath adsorption experiment was first conducted using the as-synthesized zeolite A for comparison. Simultaneously, the as-synthesized Fe_3O_4/ZA nanocomposite with different Fe_3O_4 NP loadings was conducted in the same condition for evaluating the effect of Fe_3O_4 NPs (wt. %) loading on MB removal. For investigating the removal efficiency and adsorption capacity of the Fe_3O_4/ZA nanocomposite, two separate groups of samples 3.3% Fe_3O_4/ZA and 6.6% Fe_3O_4/ZA were used for the bath adsorption experiments. The experiments were conducted with a series of samples by applying the same experimental parameters, and the supernatant of each sample was collected at different adsorption time (interaction time) from 10 to 240 minutes. Each adsorption experiment was conducted with three replications. The average data were used to plot in the UV-VIS graphs.

3. Results and Discussion

3.1. Microstructure of Magnetic Fe_3O_4/ZA Nanocomposite. The formation and crystalline structures of the as-synthesized magnetic Fe_3O_4/ZA nanocomposite, magnetic Fe_3O_4 NPs, and ZA can be well characterized by X-ray diffraction (XRD) analysis. The XRD analysis is based on Bragg's equation $n\lambda = 2\,d\,\sin\,\theta$ [31], where n is the order of diffraction, λ is the wavelength of incident X-ray (Cu $K\alpha$, 0.15406 nm), d or d_{hkl} is the interplanar (hkl) spacing, and θ is the angle between the incident X-ray and the scattering planes. XRD patterns of the Fe_3O_4/ZA nanocomposite, Fe_3O_4 NPs, and ZA samples are shown in Figure 2. For the as-synthesized ZA, the presence of characteristic peaks located at 2θ ~7.3°, 10.3°, 16.3°, 21.9°, 24.2°, 27.4°, 29.9°, and 34.3° matched well with standard diffraction peaks of (100), (110), (111), (210), (300), (311), (321), (330), and (332) planes of zeolite NaA (zeolite A, (Na) JCPDS # 00-038-0241). These observed peaks indicate the existence of zeolite A (Linde Type A) [32] crystalline phase in the sample and well agreed with previous reports [25, 33].

The XRD pattern of the as-prepared Fe_3O_4 NPs shows the diffraction peaks located at 2θ ~18.7°, 31.3°, 35.6°, 43.3°, 45.1°, 53.6°, 57.3°, and 62.9° correspond to diffraction peaks of (111), (200), (311), (400), (422), (511), and (440) planes of Fe_3O_4 crystalline phase (Fe_3O_4 magnetic, JCPDS #00-065-0731). These characteristic peaks confirm the dominance of Fe_3O_4 magnetic phase [25, 27] in the sample. The formation mechanism of Fe_3O_4 NPs can be explained by the reaction of Fe^{2+}/Fe^{3+} in the hydrothermal reaction as follows:

$$Fe^{2+} + 2Fe^{3+} + 8OH^- \longrightarrow Fe_3O_4 + 4H_2O. \quad (7)$$

For the Fe_3O_4/ZA nanocomposite samples with different Fe_3O_4 loadings (3.3, 6.6, and 9.3 wt.%), the presence of

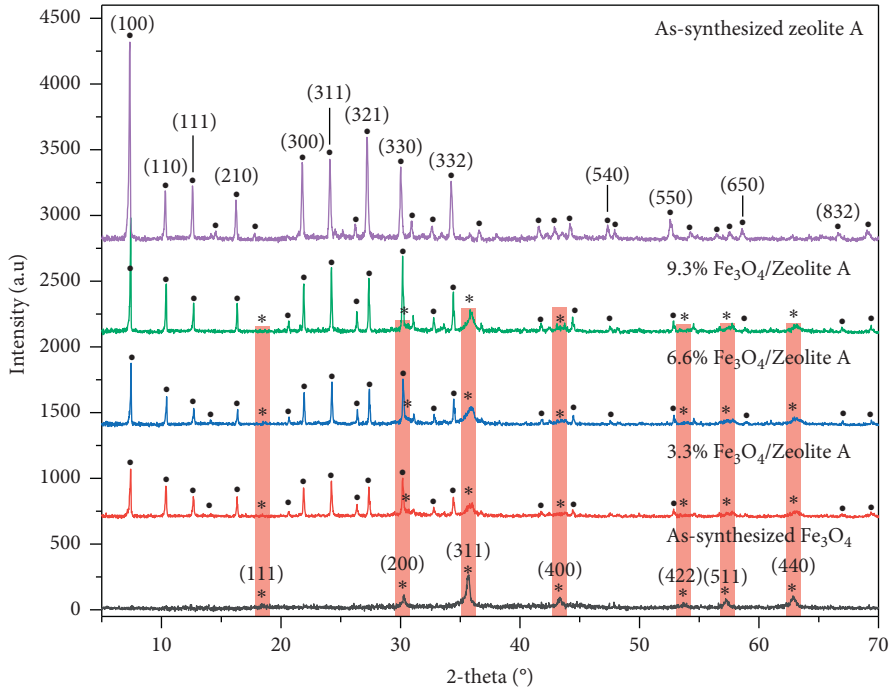

FIGURE 2: XRD patterns of ZA powder, Fe_3O_4 NP, and Fe_3O_4/ZA nanocomposite samples with different Fe_3O_4 NP loadings (wt. %).

characteristic peaks centered at 2θ ~18.8°, 30.3°, 35.6°, 43.5°, 57.3°, and 63.2° corresponds to (111), (200), (311), (400), (511), and (440) planes of Fe_3O_4 crystalline phase (JCPDS #00-065-0731) indicating that Fe_3O_4 magnetic phase has been successfully incorporated on the ZA matrix and forming Fe_3O_4/ZA nanocomposite. The crystallite size along a specific (hkl) direction of Fe_3O_4/ZA nanocomposite, ZA, as well as magnetic Fe_3O_4 samples can be calculated using Scherrer's equation [34] (equation (8)) with accepted shape factor of $K = 0.94$. Scherrer's equation is given as follows:

$$D_{(\mathrm{hkl})} = \frac{0.94\lambda}{\beta \cos \theta}, \tag{8}$$

where λ is the wavelength of X-ray radiation (Cu $K\alpha = 1.5406$ nm), β is the full width at half maximum (FWHM), θ is the diffraction angle, and $D_{(\mathrm{hkl})}$ is the average crystallite size. By applying Scherrer's equation, the crystallite size ($D_{(311)}$) for (311) peak of Fe_3O_4 NPs was calculated to be ~19.1 nm while the crystallite size of ZA calculated for (100) is ~96.5 nm. The crystallite size of the Fe_3O_4/ZA nanocomposite and magnetic Fe_3O_4 phases of the as-synthesized composite samples is listed in Table 1.

As a powerful characterization technique, Raman analysis offers us more information about the structure of aluminosilicate zeolitic materials [35] and the magnetic phase of iron oxides [36]. As seen in Figure 3, Lorentz fitting of the micro-Raman spectrum of ZA sample exhibits Raman vibration modes located at ~109.5, 164.4, 279.4, 341.6, 475.7, 716.9, 970.2, 1041.4, and 1099.8 cm^{-1}. The strongest bands located at ~475.7 cm^{-1} are assigned to the bending mode of 4-membered Si–O–Si rings (4MR) [37, 38]. While the Raman bands at ~341.6 and ~408.3 cm^{-1} are attributed to the bending mode of 6-membered Si–O–Si rings (6MR), the Raman bands at ~970.2, 1041.4, and 1099.8 cm^{-1} are attributed to the asymmetric T–O–T (T ≡ Si or Al) stretching motions [37, 38]. Interestingly, the band at ~109.5 cm^{-1} is attributed to the bending mode of higher membered rings, such as 8-membered rings (8MR) of zeolite A that also observed in previously reports [39]. In case of Fe_3O_4 NPs sample, Raman spectrum reveal the dominant bands centered at ~221.6, 270.2, 379.6, 476.9, 647.3, and 1256.9 cm^{-1} of the Fe_3O_4 NPs. These peaks are well agreed with previous reports [37, 38] that confirm the magnetic phase of the as-synthesized Fe_3O_4 NPs. Careful investigation the Raman spectra of the Fe_3O_4/ZA nanocomposite samples with different Fe_3O_4 NP mass loadings show that all the spectra exhibit three dominant Raman bands at ~270, 565 and ~637–648 cm^{-1}, which correspond to the E_g, T_{2g}, *and* A_{1g} modes of magnetic Fe_3O_4 phase [40], respectively. These observations help confirm the Fe_3O_4/ZA nanocomposite has been successfully synthesized.

3.2. Surface Morphology of Fe_3O_4/ZA Nanocomposite. The surface morphologies of the as-synthesized Fe_3O_4/ZA nanocomposite, Fe_3O_4 NPs and ZA samples were observed using FESEM, as shown in Figure 4. As seen in Figures 4(a)–4(c), the surface morphology of the ZA sample is dominated with characteristic cubic shape and relatively shiny edges. The crystallite sizes in range of ~5–10 μm with well-defined and smooth edges display the typical cubic morphology of LTA zeolites that can be clearly observed.

In Figures 4(g)–4(i), particles that are more spherical in shape and significantly smaller in dimension are evident in the FESEM images and defined the typical morphology of Fe_3O_4 nanoparticles. The magnetic crystalline phase of the Fe_3O_4

Table 1: Calculated crystallite size of the as-synthesized ZA and magnetic Fe_3O_4 phases.

Sample (s)	Crystallite size $D_{(hkl)}$ (nm)		S_{BET} ($m^2 \cdot g^{-1}$)	Pore volume ($cm^3 \cdot g^{-1}$)	Pore radius (nm)
	ZA phase (100)	Fe_3O_4 phase (311)			
Zeolite A	96.47	—	56.49	0.200	1.21
9.3% Fe_3O_4/ZA	161.81	15.24	117.04	0.154	0.74
6.6% Fe_3O_4/ZA	158.02	11.84	116.98	0.125	0.73
3.3% Fe_3O_4/ZA	117.41	11.89	63.18	0.128	0.63
Fe_3O_4 NPs	—	19.08	5.97	0.017	0.33

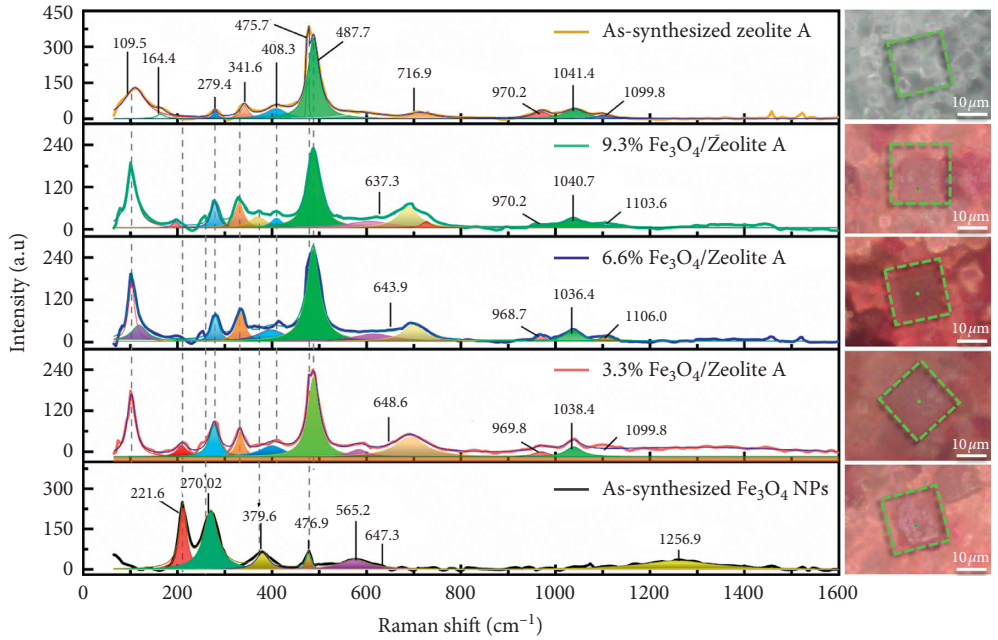

Figure 3: Micro-Raman spectra of zeolite A as-synthesized Fe_3O_4 NPs and Fe_3O_4/ZA nanocomposite samples with different Fe_3O_4 NP loadings (wt. %). The optical microscope images of the probed area (dash rectangles) are presented right next to their corresponding spectrum.

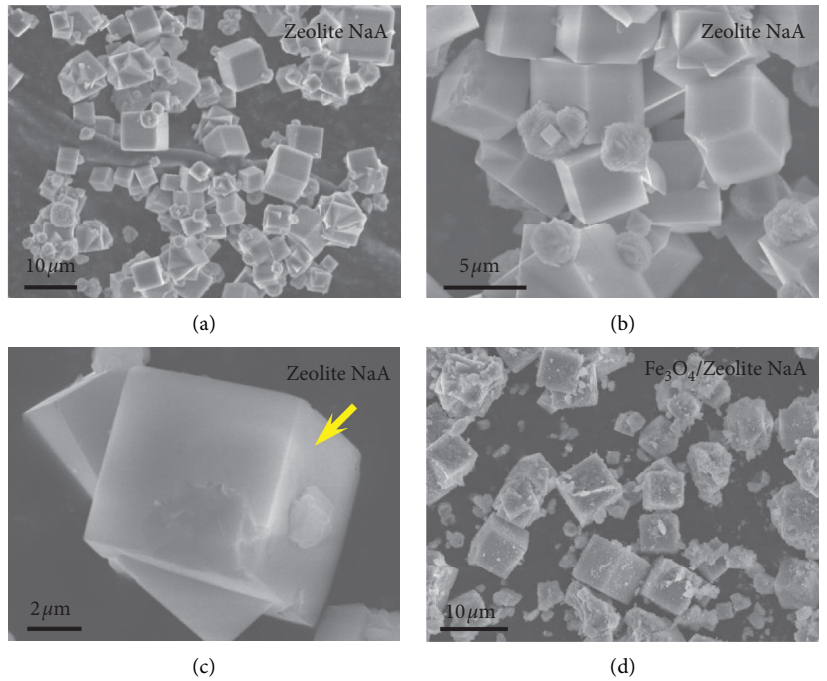

Figure 4: Continued.

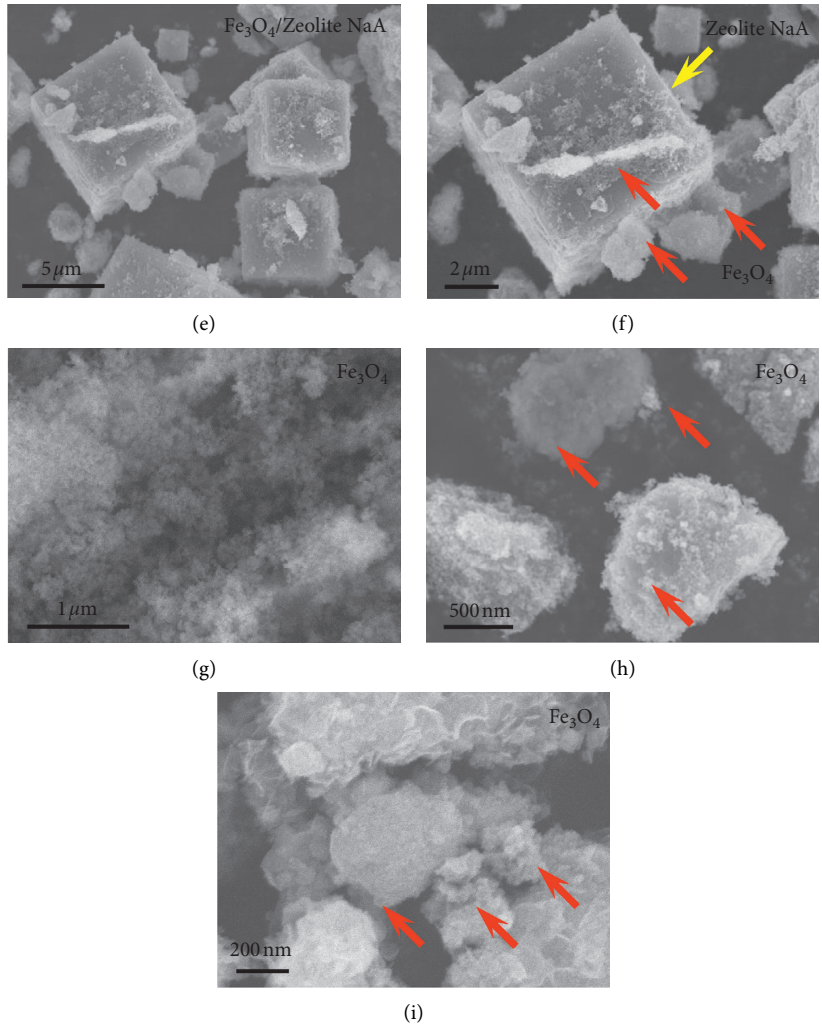

Figure 4: FESEM images of the as-synthesized zeolite A (a–c), 3.3% Fe_3O_4/zeolite A nanocomposite (d–f), and Fe_3O_4 NPs (g–i).

nanoparticles has been clearly confirmed with XRD results (Figure 2) and Raman analysis (Figure 3). The introduction of Fe_3O_4 NPs into the zeolite A structures lead to noticeable changes in the surface morphology, as shown in Figures 4(d)–4(f). After decorated with Fe_3O_4 NPs, the surface of 3.3% Fe_3O_4/ZA nanocomposite sample is covered with nanoparticles that occupy porous surface structure. The porous surface morphology may lead to the increasing of specific surface area (SSA) (Table 1) and facilitating the adsorption capability of the as-synthesized (~3.3–9.3%) Fe_3O_4/ZA nanocomposite samples (SSA ~63.18–117.04 $m^2 \cdot g^{-1}$) when compared with that of bare zeolite A (~56.49 $m^2 \cdot g^{-1}$) and Fe_3O_4 NPs (~5.97 $m^2 \cdot g^{-1}$).

3.3. Chemical Composition. Energy-dispersive X-ray (EDX) was employed to analyze the chemical composition of the as-synthesized 3.3% Fe_3O_4/ZA nanocomposite and Fe_3O_4 NP samples. The EDX spectra (Figures 5(b) and 5(d)) were recorded in the area shown in Figures 5(a) and 5(c) (SEM images).

EDX spectra in Figure 5(d) show that the main chemical composition of Fe_3O_4 NPs sample is Fe (41.67%) and O (57.33%) characterized by two peaks located at binding energy (Fe $K\alpha$) ~6.46 and ~7.08 keV, whereas the main elemental compositions of the Fe_3O_4/ZA nanocomposite sample are include O (53.38%), Na (8.8%), Al (6.82%), Si (7.40%), and Fe (6.96%). In addition, the appeared peaks in regions of ~6.46 and ~7.08 keV are originated from the binding energies of Fe Kα indicating the existence of iron in the sample. The calculated Fe/O ratio is ~0.73 that is matched well with the stoichiometric ratio (Fe/O = 0.75) of Fe_3O_4 oxide which indicates the presence of magnetic iron oxide in the as-synthesized sample. Also, from the EDX results, the calculated Si/Al ratio of the as-synthesized Fe_3O_4/ZA nanocomposite is ~0.940 that is close to the stoichiometric Si/Al ratio of zeolite A (Si/Al = 0.925). The presence of iron and oxygen further confirmed the dominance of magnetite nanoparticles in the nanocomposite.

3.4. Fourier-Transform Infrared Spectroscopy (FTIR) Analysis. FTIR analysis provides more information about the structures of the as-synthesized Fe_3O_4/ZA nanocomposite because it reveals the characteristic vibrational bands of the

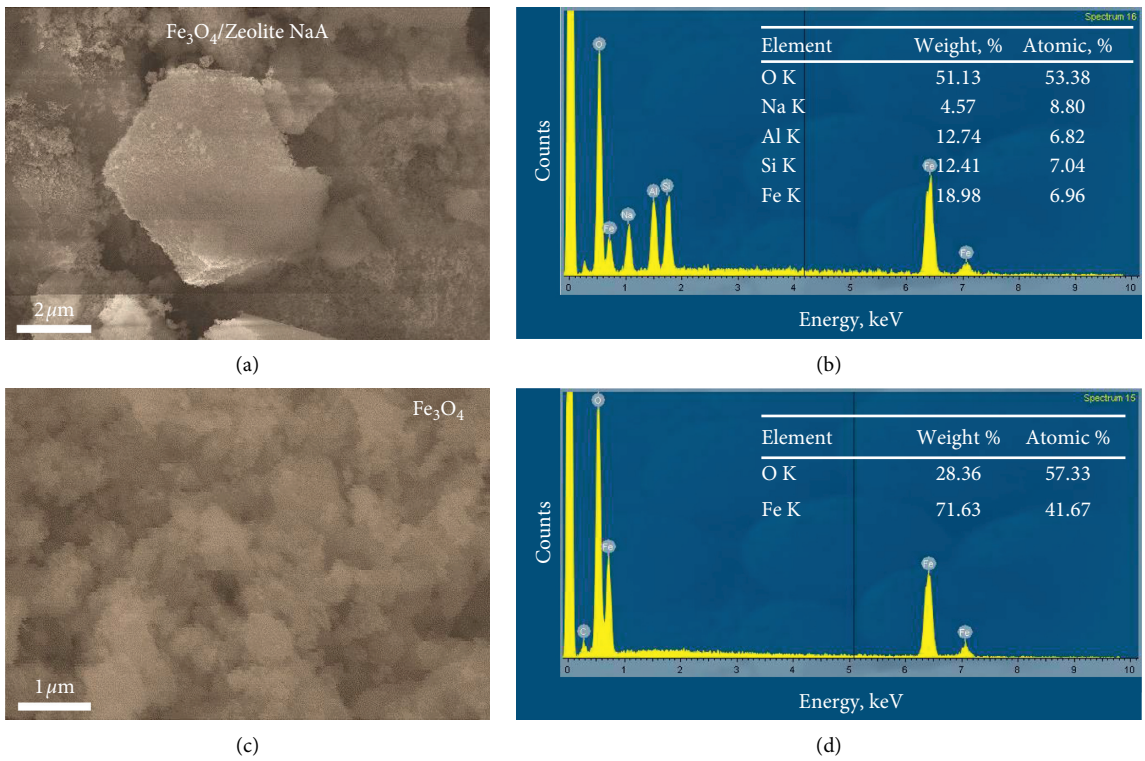

Figure 5: FESEM images and EDX spectra of 3.3% Fe_3O_4/ZA nanocomposite (a, b) and Fe_3O_4 NP (c, d) samples, respectively.

functional groups dominating in their structures, as shown in Figure 6. The FTIR absorption peaks located at ~3360–3510 cm^{-1} indicate the presence of the characteristic hydroxyl group (–OH) of the water on the as-synthesized Fe_3O_4/ZA composite zeolite A and Fe_3O_4 NPs [41].

In the FTIR spectra of the Fe_3O_4/ZA nanocomposite and ZA samples, the peaks centered at ~1630 cm^{-1} can be attributed to the vibration bending modes of coordinated (–OH) groups attached on the surfaces of zeolite A crystals [41]. The vibration band occuring at ~1090 cm^{-1} and 986 cm^{-1} represents the internal vibrations due to the asymmetric stretching of Si–O–Al tetrahedral [41]. In addition, the spectra at ~660 cm^{-1} of the zeolite A samples can be attributed to internal vibrations due to symmetric stretching within the zeolite structure. The presence of the external T–O linkage, caused by the double ring [29], is also confirmed by the band at the wavenumber of ~550 cm^{-1}. The band at position ~466 cm^{-1} indicates the presence of internal tetrahedron vibrations of Si–O and Al–O with bending modes of the sodalite cages found in zeolites [29].

For the as-synthesized Fe_3O_4/ZA nanocomposite, the presence of Fe_3O_4 NPs leads to the variation of vibration band of the zeolite A. The absorption peaks centered at ~760 cm^{-1} (in sample 3.3% Fe_3O_4/ZA), ~730 cm^{-1} (in sample 6.6% Fe_3O_4/ZA), and ~660 cm^{-1} (in sample 9.3% Fe_3O_4/ZA) correspond to Fe^{2+}–O–Fe^{3+}, Fe^{3+}–O, and Fe^{2+}–O bonds from Fe_3O_4 which also reported previously [42–44]. Those peaks did not appear in the zeolite A spectrum but presented the spectrum of Fe_3O_4 sample. This observation suggests that the Fe_3O_4 NPs have been introduced to the zeolite A structure.

3.5. Selective Adsorption Removal of Methylene Blue

3.5.1. Effect of Fe_3O_4 Loading on Fe_3O_4/ZA Nanocomposite on the Removal of MB. The adsorption capacity and the effect of Fe_3O_4 NPs mass loading on the Fe_3O_4/ZA nanocomposite to the removal of MB were evaluated by determining the UV-VIS absorbance spectra of the as-synthesized Fe_3O_4/ZA and zeolite A samples. As seen in Figure 7(a), the absorbance spectrum of the as-synthesized ZA shows a significant decrease in the intensity and total sum of area under the fitted peaks at wavelength 664 nm compared to that of the initial MB solution. The calculated adsorption capacity (q_e, mg·g^{-1}) and the MB removal efficiency (R, %) of ZA sample are ~32.99 mg·g^{-1} and ~79.11%, respectively, which were close to those of the previously reports [20] (Table 2).

For the Fe_3O_4/ZA nanocomposite samples, the corresponding UV-VIS spectra indicate the adsorption capacity of Fe_3O_4/ZA nanocomposites through the decrease in intensity of characteristic absorbed peaks of MB (Figures 1 and 7(a)) and total sum of area under fitted peaks (Table 2). The adsorption capacity and the removal efficiency increase from ~81.90 to ~94.93% and ~34.12 to ~39.56 mg·g^{-1}, respectively, when loading of Fe_3O_4 NP increases from ~3.3 to ~6.6% wt. These calculated values are significantly high when compared to that of the ZA sample (this work) and magnetic iron (Fe_3O_4) mud previously reported by Liu et al. (~27.4 mg·g^{-1}

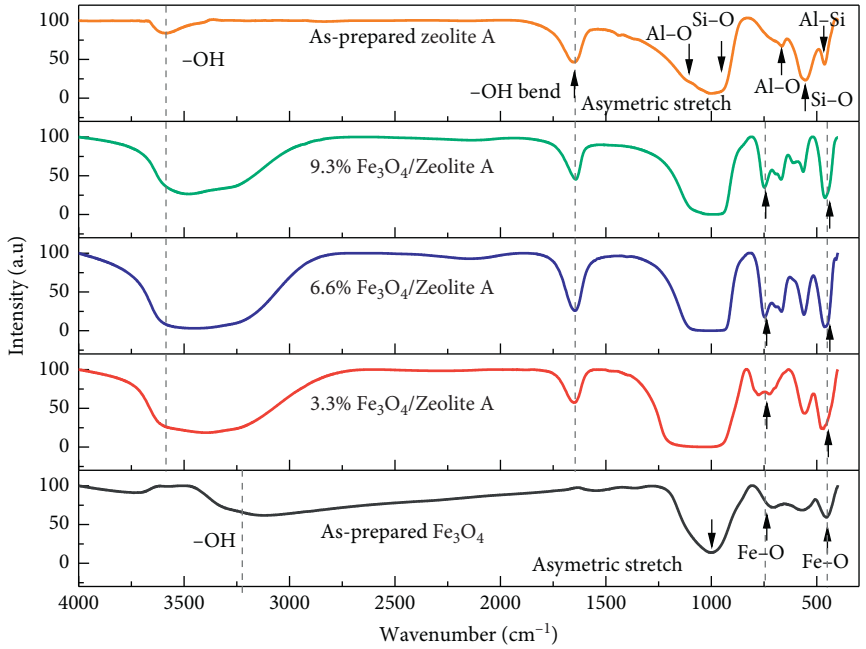

Figure 6: FTIR spectra of zeolite A Fe_3O_4 NPs and Fe_3O_4/ZA nanocomposite samples with different Fe_3O_4 NP loadings (wt. %).

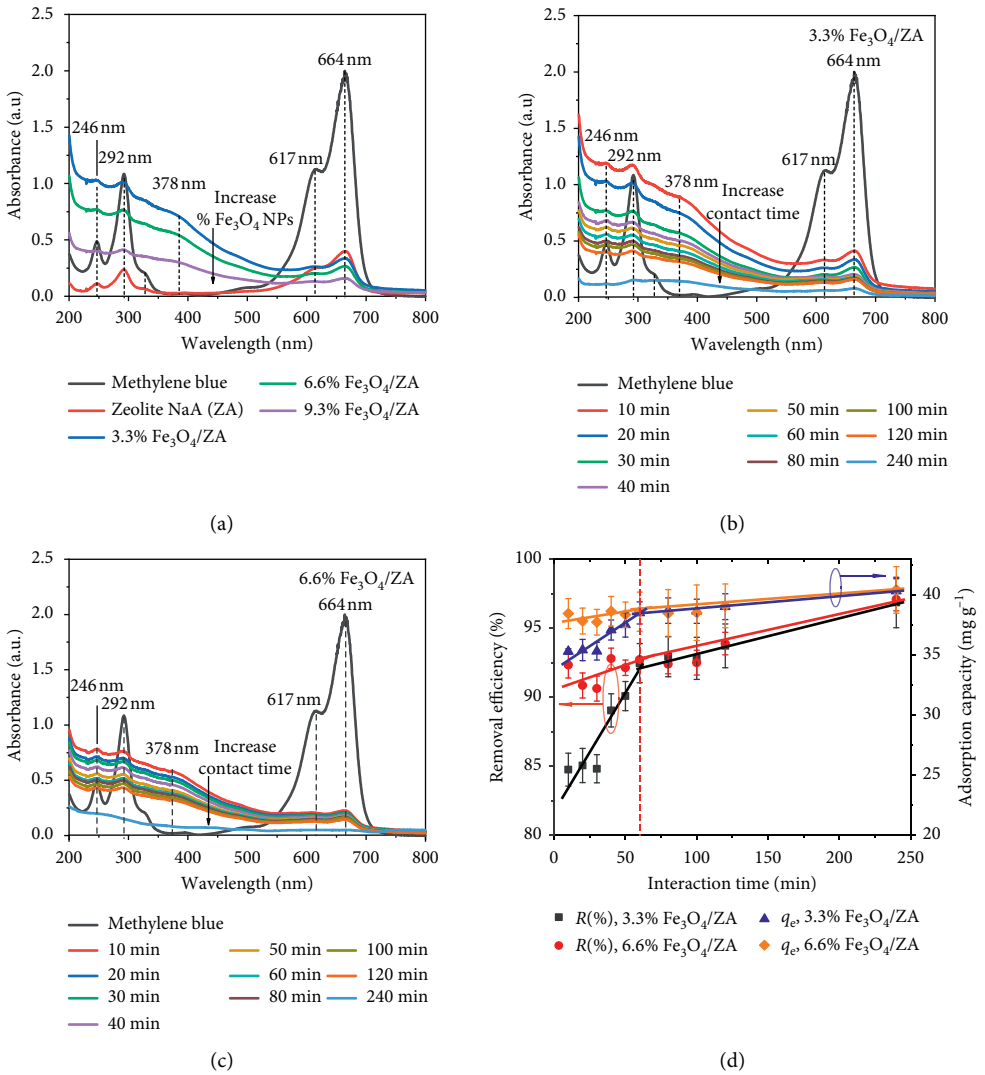

Figure 7: Continued.

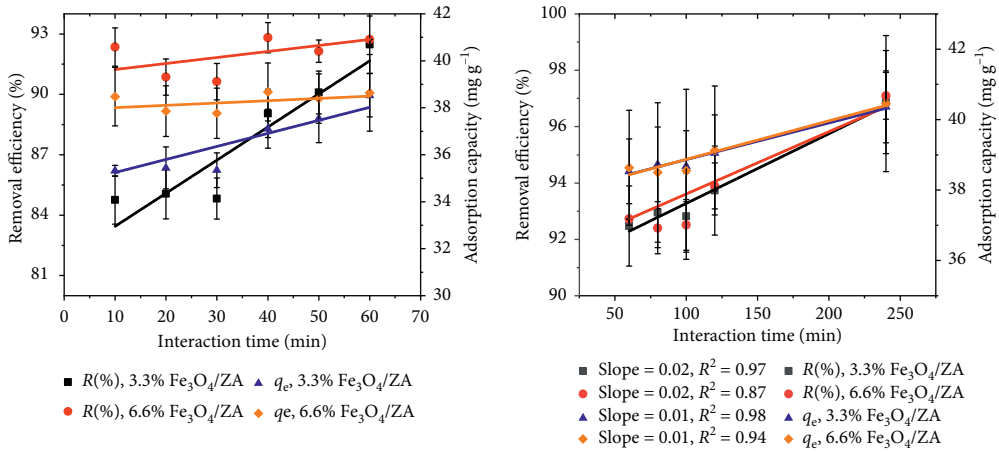

Figure 7: UV-VIS absorbance spectra of supernatants collected from batch adsorption experiments. (a) The absorbance spectra of the MB solution treated by Fe_3O_4/ZA nanocomposite with different Fe_3O_4 NP loadings; (b, c) absorbance spectra of 3.3% Fe_3O_4/ZA and 6.6% Fe_3O_4/ZA samples at different interaction (adsorption) times; (d) removal efficiency (R, %) and adsorption capacity (q_e, mg·g^{-1}) of 3.3% Fe_3O_4/ZA and 6.6% Fe_3O_4/ZA samples, respectively; linear fitting results of removal efficiency and adsorption capacity in adsorption ranges of 0–60 minutes (e) and 60–240 minutes (f) in (d); the experiments data are presented as solid dots with error bars, while solid lines are linear fitting results of experiments data in Figures 7d, 7e, and 7f.

Table 2: Effect of Fe_3O_4 loading to the adsorption capacity and removal efficiency of the as-synthesized Fe_3O_4/ZA nanocomposite.

Samples	Total area under fitted peaks	q_e (mg·g^{-1})	R (%)
9.3% Fe_3O_4/ZA	11.54 ± 2.75	39.56 ± 0.34	94.93 ± 0.87
6.6% Fe_3O_4/ZA	22.81 ± 1.34	37.49 ± 0.35	89.98 ± 0.93
3.3% Fe_3O_4/ZA	41.23 ± 3.37	34.12 ± 0.28	81.90 ± 0.84
Zeolite A	47.40 ± 1.99	32.99 ± 0.29	79.19 ± 0.90

[27]). The high adsorption capacity and the removal efficiency indicate the strong effect of Fe_3O_4 NP loading on the as-synthesized Fe_3O_4/ZA nanocomposite [45]. The maximum adsorption capacity of the as-synthesized Fe_3O_4/ZA nanocomposite (~40.46 mg·g^{-1}) is rather high than that reported with Z-Fe_3O_4 NCs adsorbent (~1.15 mg·g^{-1}) [13], magnetic zeolite HY-Fe_3O_4 (~28.41 mg·g^{-1}), zeolite 13X-Fe_3O_4 (~28.41 mg·g^{-1}) [46], and magnetic NaY zeolite composite (~2.045 mg·g^{-1}) [47]. The maximum adsorption capacity of various adsorbents reported for MB removal from aqueous solution is listed in Table 3.

It can also be observed that the Fe_3O_4/ZA nanocomposite samples exhibit absorbance peaks centered at ~378 nm and large absorbed background compared to that of ZA sample. The absorbance peaks of Fe_3O_4/ZA nanocomposite samples can be originated from $FeCl_4^-$ [48] and ≡$FeOH_2^+$, ≡FeOH, and ≡FeO^- complexes forming from electrostatic interaction between ferric (III) surface ions in Fe_3O_4 NPs and Cl^- ions in MB molecules as well as OH^- ions in alkaline condition. In addition, functional groups such as ≡$FeOH_2^+$, ≡FeOH, and ≡FeO^- interact with Na^+ on ZA surfaces to form (≡FeO–Na^+) through electrostatic forces that could be favourably replaced by MB. Therefore, the possible adsorption mechanism for the removal of MB can be explained by the following equations:

$$\equiv \mathrm{FeOH} + \mathrm{NaOH} \longrightarrow \equiv \mathrm{FeONa} + \mathrm{H_2O}, \quad (9)$$

$$\equiv \mathrm{FeONa} + \mathrm{MB} \longrightarrow \equiv \mathrm{FeOMB^+} + Na^+. \quad (10)$$

This observation provides strong evidence that support for the adsorption removal capability of the as-synthesized Fe_3O_4/ZA nanocomposite.

3.5.2. Adsorption Capability versus the Contact Time. The effect of interaction time (or adsorption time) on removal of MB by the as-synthesized Fe_3O_4/ZA nanocomposite is shown in Figures 7(b), and 7(c). The batch adsorption experiments were conducted with two groups of samples including 3.3% Fe_3O_4/ZA and 6.6% Fe_3O_4/ZA nanocomposite for comparison. As seen in Figure 7(c), the absorbance spectra of sample 3.3% Fe_3O_4/ZA nanocomposite show that the absorbance intensity of MB remains in the supernatants were decreased significantly. The

Table 3: Comparison of the maximum adsorption capacity of various adsorbents for MB removal.

Materials	Adsorbent dose ($g{\cdot}L^{-1}$)	Time (min)	Dye (MB) concentration C_o ($mg{\cdot}L^{-1}$)	q_e ($mg{\cdot}g^{-1}$)	R (%)	Ref.
Fe_3O_4/ZA nanocomposite	7.2	120	300.0	40.46	97.9	This work
Z-Fe_3O_4 NCs	0.8	120	10	1.15	82.6	[20]
Magnetic iron (Fe_3O_4) mud	5.0	120	100	27.4	93.0	[27]
Zeolite HY-Fe_3O_4	0.3–1.2	—	10–40	28.41	87.8	[46]
Zeolite 13X-Fe_3O_4	0.3–1.2	—	10–40	29.20	83.1	[46]
Magnetic NaY zeolite composite	46.2	45	10	2.045	98.4	[47]

decrease in the absorbance indicates that a large concentration of MB molecules was removed from the initial solutions. The experimental data of removal efficiency R (%) and adsorption capacity q_e ($mg{\cdot}g^{-1}$) of samples 3.3% Fe_3O_4/ZA and 6.6% Fe_3O_4/ZA nanocomposite were plotted with errors bars as seen in Figure 7(d). The R and q_e values were obtained to be ~84.76% and ~35.3 $mg{\cdot}g^{-1}$ after 10 minutes and increased to ~92.47% and ~38.5 $mg{\cdot}g^{-1}$, after 60 minutes, respectively. The R and q_e values increase with an increasing of interaction time and reach to ~96.87% and ~40.36 $mg{\cdot}g^{-1}$ after 240 minutes, as seen in Figure 7(e). When the amount of Fe_3O_4 loading increased to ~6.6% wt. as in samples 6.6% Fe_3O_4/ZA nanocomposite, the R and q_e values of these samples were observed to increase significantly to ~92.35% and ~38.48 $mg{\cdot}g^{-1}$ at about 10 minutes of adsorption. At 60 minutes of interaction, these values were calculated to be about ~92.73% and ~38.64 $mg{\cdot}g^{-1}$ and reached to ~97.89% and ~40.46 $mg{\cdot}g^{-1}$ at 240 minutes, respectively. Experiments data are provided in Table 4.

Careful analysis of the variation of the obtained experimental data are in Figure 7(d) with the linear fitting results presented in Figures 7(e) and 7(f); one can observe that the removal efficiency and adsorption capacity of the two samples versus the interaction time change significantly and can be separated in two stages of about 0–60 minutes and 60–240 minutes. The R and q_e values of the as-synthesized Fe_3O_4/ZA nanocomposite samples in the first stages of adsorptions (lower than 60 minutes) increase nonlinearly with higher rate (slope of ~0.05–0.16; correlation factor $r^2 = 0.42$–0.86), while in the second stage, these values increase linearly with lower rate (slope of ~0.01–0.12 and $r^2 = 0.87$–0.98). The R and q_e values obtained in second stage suggests that the adsorption removal of MB follows a kinetic adsorption model of pseudo-second-order [20] which involves both physical and chemical interactions. The phenomenon can be explained by considering the surface structure and morphology of the as-synthesized Fe_3O_4/ZA nanocomposite (Figure 4). The incorporation of Fe_3O_4 particles in to zeolite NaA structure leads to the increase in a large number of active sites that can interact with MB molecules. At the first stage of adsorption, with a large number of available active sites, the adsorption process occurred simultaneously in the MB solution leading to the increase in adsorption capacity. It was also noticed that the rate of adsorption (slopes of the fitted lines) decreased after 60 minutes indicating that the availability of active sites on Fe_3O_4/ZA nanocomposite surfaces for the MB molecules to occupy had been reduced at equilibrium adsorption condition. The kinetic adsorption model of pseudo-second-order is defined by the following equations [27]:

$$\frac{dq}{dt} = k_2 (q_e - q_t)^2. \tag{11}$$

The solution of equation (11) can be obtained by direct integration under the conditions: $t = 0$ and $q_t = 0$ at $t = t$ and $q_t = q_t$ as follows:

$$\frac{t}{q_t} = \frac{1}{k_2 q_e^2} + \frac{1}{q_e} t, \tag{12}$$

where q_e ($mg{\cdot}L^{-1}$) and q_t ($mg\ L^{-1}$) are the equilibrium and at (t) min adsorption capacity and k_2 ($g\ mg^{-1}{\cdot}min^{-1}$) is the pseudo-second-order diffusion rate constant that describes the amount of MB molecules adsorbed on the Fe_3O_4/ZA NCs at interaction time (t) and at equilibrium, respectively. In this regard, the values k_2 and q_e are obtained from the plot of (t/q_t) versus time (t) as listed in Table 5.

The uptake of the MB molecules by the Fe_3O_4/ZA nanocomposite can be addressed at the combination of the interaction between active sites the surfaces and edges of the Fe_3O_4 nanoparticles and zeolite NaA with the MB molecules. In this case, the invert spinel structure of the as-synthesized Fe_3O_4 NPs provides a large number of active sites (O^{2-} and Fe^{2+}/Fe^{3+}) that simultaneously electrostatically adsorbs the positive ($C_6H_{18}SN_3^+$) and negative (Cl^-) polarized poles of MB molecules, whereas the removal of MB in case of the zeolite NaA resulted from the electrostatic attraction between the cationic MB molecule and the negatively surface-charged zeolite A. Furthermore, due to the magnetic property of the as-synthesized Fe_3O_4/ZA nanocomposite, the materials can be recovered separated conveniently from aqueous solution for reuse (as seen in Figure 1(c)). Therefore, the magnetic Fe_3O_4/ZA nanocomposite is a suitable adsorbent for removal of MB from aqueous solution especially for purifying wastewater.

Table 4: Effect of interaction time to the adsorption capacity and removal efficiency of the Fe_3O_4/ZA nanocomposite.

Time (min)	3.3% Fe_3O_4/ZA			6.6% Fe_3O_4/ZA		
	Total area	q_e (mg·g^{-1})	R (%)	Total area	q_e (mg·g^{-1})	R (%)
0	227.74 ± 20.74	—	—	—	—	—
10	34.71 ± 4.31	35.32 ± 0.23	84.76 ± 1.20	17.42 ± 1.07	38.48 ± 1.25	92.35 ± 0.98
20	34.02 ± 3.90	35.44 ± 0.89	85.06 ± 1.24	20.81 ± 2.04	37.86 ± 1.08	90.86 ± 0.90
30	34.56 ± 2.86	35.34 ± 0.74	84.83 ± 1.02	21.33 ± 1.92	37.76 ± 1.07	90.63 ± 0.91
40	24.92 ± 0.32	37.11 ± 0.83	89.06 ± 1.20	16.36 ± 5.13	38.67 ± 1.23	92.82 ± 0.75
50	22.56 ± 2.51	37.54 ± 1.02	90.09 ± 1.06	17.89 ± 9.24	38.39 ± 1.05	92.14 ± 0.55
60	17.14 ± 7.12	38.53 ± 0.92	92.47 ± 1.42	16.56 ± 2.82	38.64 ± 1.63	92.73 ± 0.46
80	16.06 ± 3.42	38.73 ± 1.06	92.95 ± 1.46	17.31 ± 6.42	38.50 ± 1.98	92.40 ± 0.69
100	16.34 ± 7.14	38.68 ± 10.1	92.82 ± 1.53	17.05 ± 2.16	38.55 ± 2.31	92.51 ± 0.89
120	14.27 ± 1.02	39.06 ± 1.08	93.73 ± 1.58	13.89 ± 3.82	39.12 ± 1.83	93.90 ± 0.81
240	7.13 ± 2.86	40.36 ± 1.02	96.87 ± 1.83	6.62 ± 3.51	40.46 ± 1.93	97.89 ± 0.83

Table 5: Kinetic constants of pseudo-second-order predicted models for two groups of Fe_3O_4/ZA NCs.

Kinetic model	Model parameters	3.3% Fe_3O_4/ZA	6.6% Fe_3O_4/ZA
Pseudo-second-order	q_e (mg·L^{-1})	99.575	99.601
	k_2	0.00286	0.00316
	r^2	0.98	0.94

4. Conclusions

In conclusion, we have successfully synthesized and characterized the Fe_3O_4/zeolite NaA nanocomposite for potential adsorption removal of methylene blue in term of wastewater treatment. The as-synthesized Fe_3O_4/ZA nanocomposite exhibited a high adsorption capacity and removal efficiency compared to those of the as-synthesized zeolite NaA in the same experimental condition. The adsorption mechanism of MB molecules by the Fe_3O_4/ZA nanocomposite can be addressed at the combination of the interaction between active sites the surfaces and edges of the Fe_3O_4 spinel-structured nanoparticles and zeolite NaA with the MB molecules. With a small loading of ~3.3% Fe_3O_4, the removal efficiency reaches up to ~96.8% and ~40.36 mg·g^{-1} of adsorption capacity. The removal efficiency and the adsorption capacity were observed to increase linearly with the slightly increasing of adsorption time and Fe_3O_4 NP loading in the as-synthesized nanocomposites. Our results underscore the feasibility of magnetic zeolite nanocomposite materials as a lower cost adsorbent for the application of wastewater purification.

Data Availability

Some data used to support the findings of this study are included in the tables and graphs within the article. More data (Excel files and unedited images) are available from the corresponding author upon reasonable request.

Disclosure

This research received no external funding.

Conflicts of Interest

The authors declare that there are no conflicts of interest regarding the publication of this paper.

Acknowledgments

The authors would like to thank Ho Chi Minh City University of Technology (HCMUT), VNU-HCM, and Tra Vinh University for the support of time and facilities for this study.

References

[1] V. K. Gupta, I. Ali, and V. K. Saini, "Removal of rhodamine B, fast green, and methylene blue from wastewater using red mud, an aluminum industry waste," *Industrial & Engineering Chemistry Research*, vol. 43, no. 7, pp. 1740–1747, 2004.

[2] K. Mahapatra, D. S. Ramteke, and L. J. Paliwal, "Production of activated carbon from sludge of food processing industry under controlled pyrolysis and its application for methylene blue removal," *Journal of Analytical and Applied Pyrolysis*, vol. 95, pp. 79–86, 2012.

[3] A. K. Verma, R. R. Dash, and P. Bhunia, "A review on chemical coagulation/flocculation technologies for removal of colour from textile wastewaters," *Journal of Environmental Management*, vol. 93, no. 1, pp. 154–168, 2012.

[4] S. Yu, M. Liu, M. Ma, M. Qi, Z. Lü, and C. Gao, "Impacts of membrane properties on reactive dye removal from dye/salt mixtures by asymmetric cellulose acetate and composite polyamide nanofiltration membranes," *Journal of Membrane Science*, vol. 350, no. 1-2, pp. 83–91, 2010.

[5] A. Asghar, A. A. Abdul Raman, and W. M. A. Wan Daud, "Advanced oxidation processes for in-situ production of hydrogen peroxide/hydroxyl radical for textile wastewater treatment: a review," *Journal of Cleaner Production*, vol. 87, pp. 826–838, 2015.

[6] E. Kordouli, K. Bourikas, A. Lycourghiotis, and C. Kordulis, "The mechanism of azo-dyes adsorption on the titanium dioxide surface and their photocatalytic degradation over samples with various anatase/rutile ratios," *Catalysis Today*, vol. 252, pp. 128–135, 2015.

[7] M. T. Yagub, T. K. Sen, S. Afroze, and H. M. Ang, "Dye and its removal from aqueous solution by adsorption: a review," *Advances in Colloid and Interface Science*, vol. 209, pp. 172–184, 2014.

[8] Ü. Geçgel, G. Özcan, and G. Ç. Gürpınar, "Removal of methylene blue from aqueous solution by activated carbon prepared from Pea shells (*pisum sativum*)," *Journal of Chemistry*, vol. 2013, Article ID 614083, 9 pages, 2013.

[9] M. Khodaie, N. Ghasemi, B. Moradi, and M. Rahimi, "Removal of methylene blue from wastewater by adsorption onto $ZnCl_2$ activated corn husk carbon equilibrium studies," *Journal of Chemistry*, vol. 2013, Article ID 383985, 6 pages, 2013.

[10] J. R. Guarín, J. C. Moreno-Pirajan, and L. Giraldo, "Kinetic study of the bioadsorption of methylene blue on the surface of the biomass obtained from the Algae *D. Antarctica*," *Journal of Chemistry*, vol. 2018, Article ID 2124845, 12 pages, 2018.

[11] R. Tang, C. Dai, C. Li, W. Liu, S. Gao, and C. Wang, "Removal of methylene blue from aqueous solution using agricultural residue Walnut shell: equilibrium, kinetic, and thermodynamic studies," *Journal of Chemistry*, vol. 2017, Article ID 8404965, 10 pages, 2017.

[12] N.-E. Alireza and S.-G. Zahra, "Photodegradation of methyl green by nickel-dimethylglyoxime/ZSM-5 zeolite as a heterogeneous catalyst," *Journal of Chemistry*, vol. 2013, Article ID 104093, 11 pages, 2013.

[13] R.-B. Alvaro, E. Rodrigo, G. Maykel, R. Gerardo, and R. Pérez, "Preparation and characterization of natural zeolite modified with iron nanoparticles," *Journal of Nanomaterials*, vol. 2015, Article ID 364763, 8 pages, 2015.

[14] E. R. León, E. L. Rodríguez, C. R. Beas, P.-V. Germán, and R. A. I. Palomares, "Study of methylene blue degradation by gold nanoparticles synthesized within natural zeolites," *Journal of Nanomaterials*, vol. 2016, Article ID 9541683, 10 pages, 2016.

[15] C. Baerlocher, L. B. McCusker, and D. H. Olson, *Atlas of Zeolite Framework Types*, Elsevier, Amsterdam, the Netherlands, 6th edition, 2007.

[16] T. B. Reed and D. W. Breck, "Crystalline zeolites. II. crystal structure of synthetic zeolite, type A," *Journal of the American Chemical Society*, vol. 78, no. 23, pp. 5972–5977, 1956.

[17] P. Chutia, S. Kato, T. Kojima, and S. Satokawa, "Arsenic adsorption from aqueous solution on synthetic zeolites," *Journal of Hazardous Materials*, vol. 162, no. 1, pp. 440–447, 2009.

[18] T. Gebremedhin-Haile, M. T. Olguín, and M. Solache-Ríos, "Removal of mercury ions from mixed aqueous metal solutions by natural and modified zeolitic minerals," *Water, Air, and Soil Pollution*, vol. 148, no. 1/4, pp. 179–200, 2003.

[19] S. Waghmare, T. Arfin, S. Rayalu et al., "Adsorption behaviour of modified zeolite as novel adsorbents for fluoride removal from drinking water: surface phenomena, kinetics and thermodynamics studies," *International Journal of Innovative Research in Science, Engineering and Technology*, vol. 4, pp. 4114–4124, 2015.

[20] E. Nyankson, J. Adjasoo, J. K. Efavi et al., "Characterization and evaluation of zeolite A/Fe_3O_4 nanocomposite as a potential adsorbent for removal of organic molecules from wastewater," *Journal of Chemistry*, vol. 2019, Article ID 8090756, 13 pages, 2019.

[21] J. J. Pluth and J. V. Smith, "Accurate redetermination of crystal structure of dehydrated zeolite A. absence of near zero coordination of sodium. Refinement of silicon, aluminum-ordered superstructure," *Journal of the American Chemical Society*, vol. 102, no. 14, pp. 4704–4708, 1980.

[22] R. M. Cornell and U. Schwertmann, *The Iron Oxides: Structure, Properties, Reactions, Occurrences and Uses*, John Wiley & Sons, Hoboken, NJ, USA, 2003.

[23] Y. Xiaotun, X. Lingge, N. S. Choon, and C. S. O. Hardy, "Magnetic and electrical properties of polypyrrole-coated-Fe_2O_3 nanocomposite particles," *Nanotechnology*, vol. 14, no. 6, pp. 624–629, 2003.

[24] C. Pascal, J. L. Pascal, F. Favier, M. L. Elidrissi Moubtassim, and C. Payen, "Electrochemical synthesis for the control of γ-Fe_2O_3 nanoparticle size. morphology, microstructure, and magnetic behavior," *Chemistry of Materials*, vol. 11, no. 1, pp. 141–147, 1999.

[25] H. Liu, S. Peng, L. Shu, T. Chen, T. Bao, and R. L. Frost, "Effect of Fe_3O_4 addition on removal of ammonium by zeolite NaA," *Journal of Colloid and Interface Science*, vol. 390, no. 1, pp. 204–210, 2013.

[26] D. Niznansky, N. Viart, and J. L. Rehspringer, "Nanocomposites Fe_2O_3/SiO_2-preparation by sol-gel method and physical properties," *Journal of Sol-Gel Science and Technology*, vol. 8, no. 1–3, pp. 615–618, 1997.

[27] J. Liu, Y. Yu, S. Zhu et al., "Synthesis and characterization of a magnetic adsorbent from negatively-valued iron mud for methylene blue adsorption," *PLoS One*, vol. 13, Article ID e0191229, 2018.

[28] S. Ge, X. Shi, K. Sun et al., "Facile hydrothermal synthesis of iron oxide nanoparticles with tunable magnetic properties," *The Journal of Physical Chemistry C*, vol. 113, no. 31, pp. 13593–13599, 2009.

[29] X. Zhang, D. Tang, and G. Jiang, "Synthesis of zeolite NaA at room temperature: the effect of synthesis parameters on crystal size and its size distribution," *Advanced Powder Technology*, vol. 24, no. 3, pp. 689–696, 2013.

[30] M. D. Milošević, M. Mihovil Logar, A. V. Poharc-Logar, and N. L. Jakšić, "Orientation and optical polarized spectra (380–900 nm) of methylene blue crystals on a glass surface," *International Journal of Spectroscopy*, vol. 2013, Article ID 923739, 2013.

[31] B. D. Cullity and S. R. Stock, *Elements of X-Ray Diffraction*, Prentice-Hall, New York, NY, USA, 3rd edition, 2001.

[32] M. M. J. Treacy and J. B. Higgins, *Collection of Simulated XRD Powder Patterns for Zeolites*, Elsevier on Behalf of the Structure Commission of the International Zeolite Association, Amsterdam, Netherlands, 2001.

[33] Z. Ghasemi and H. Younesi, "Preparation and characterization of nanozeolite NaA from rice husk at room temperature without organic additives," *Journal of Nanomaterials*, vol. 2011, Article ID 858961, 2011.

[34] P. Scherrer, "Bestimmung der Grösse und der inneren Struktur von Kolloidteilchen mittels," *Gottinger Nachr Maths Physics*, vol. 2, pp. 98–100, 1918.

[35] P.-P. Knops-Gerrits, D. E. De Vos, E. J. P. Feijen, and P. A. Jacobs, "Raman spectroscopy on zeolites," *Microporous Materials*, vol. 8, no. 1-2, pp. 3–17, 1997.

[36] P. C. Panta and C. P. Bergmann, "Raman spectroscopy of iron oxide of nanoparticles (Fe_3O_4)," *Journal of Material Science and Engineering*, vol. 5, no. 1, p. 217, 2015.

[37] P. K. Dutta and B. Del Barco, "Raman spectroscopy of zeolite A: influence of silicon/aluminum ratio," *The Journal of Physical Chemistry*, vol. 92, no. 2, pp. 354–357, 1988.

[38] A. Depla, E. Verheyen, A. Veyfeyken et al., "Zeolites X and A crystallization compared by simultaneous UV/VIS-Raman and X-ray diffraction," *Physical Chemistry Chemical Physics*, vol. 13, no. 30, pp. 13730–13737, 2011.

[39] P. P. H. J. M. Knops-Gerrits and M. Cuypers, "Raman spectroscopic studies of the templated synthesis of zeolites," *Studies in Surface Science and Catalysis*, vol. 142, pp. 263–270, 2002.

[40] O. N. Shebanova and P. Lazor, "Raman study of magnetite (Fe_3O_4): laser-induced thermal effects and oxidation," *Journal of Raman Spectroscopy*, vol. 34, no. 11, pp. 845–852, 2003.

[41] H. Tounsi, S. Mseddi, and S. Djemel, "Preparation and characterization of Na-LTA zeolite from Tunisian sand and aluminum scrap," *Physics Procedia*, vol. 2, no. 3, pp. 1065–1074, 2009.

[42] H. Liu, S. Peng, L. Shu, T. Chen, T. Bao, and R. L. Frost, "Magnetic zeolite NaA: synthesis, characterization based on metakaolin and its application for the removal of Cu^{2+}, Pb^{2+}," *Chemosphere*, vol. 91, no. 11, pp. 1539–1546, 2013.

[43] L. Price, K. M. Leung, and A. Sartbaeva, "Local and average structural changes in zeolite A upon ion exchange," *Magnetochemistry*, vol. 3, no. 4, p. 42, 2017.

[44] S. V. Stefanovsky, O. I. Stefanovskaya, S. E. Vinokurov, S. S. Danilov, and B. F. Myasoedov, "Phase composition, structure, and hydrolytic durability of glasses in the Na_2O-Al_2O_3-(Fe_2O_3)-P_2O_5 system at replacement of Al_2O_3 by Fe_2O_3," *Radiochemistry*, vol. 57, no. 4, pp. 348–355, 2015.

[45] A. D. J. Ruíz-Baltazar, S. Y. Reyes-López, M. D. L. Mondragón-Sánchez, A. I. R. Cortés, and R. Pérez, "Eco-friendly synthesis of Fe_3O_4 nanoparticles: evaluation of their catalytic activity in methylene blue degradation by kinetic adsorption models," *Results in Physics*, vol. 12, pp. 989–995, 2018.

[46] Z. Majid, A. A. AbdulRazak, and W. A. H. Noori, "Modification of zeolite by magnetic nanoparticles for organic dye removal," *Arabian Journal for Science and Engineering*, vol. 44, no. 6, pp. 5457–5474, 2019.

[47] M. Shirani, A. Semnani, H. Haddadi, and S. Habibollahi, "Optimization of simultaneous removal of methylene blue, crystal violet, and fuchsine from aqueous solutions by magnetic NaY zeolite composite," *Water Air and Soil Pollution*, vol. 225, no. 8, pp. 2054–2068, 2014.

[48] W. Liu, B. Etschmann, J. Brugger et al., "UV–Vis spectrophotometric and XAFS studies of ferric chloride complexes in hyper-saline LiCl solutions at 25–90°C," *Chemical Geology*, vol. 231, no. 4, 2006.